Research Article

Journal of RAMAN SPECTROSCOPY

Received: 17 June 2009 Accepted: 18 August 2009 Published online in Wiley Interscience: 12 October 2009

(www.interscience.wiley.com) DOI 10.1002/jrs.2501

Hybrid Rayleigh, Raman and two-photon excited fluorescence spectral confocal microscopy of living cells

Vishnu Vardhan Pully, Aufried Lenferink and Cees Otto*

A hybrid fluorescence–Raman confocal microscopy platform is presented, which integrates low-wavenumber-resolution Raman imaging, Rayleigh scatter imaging and two-photon fluorescence (TPE) spectral imaging, fast 'amplitude-only' TPE-fluorescence imaging and high-spectral-resolution Raman imaging. This multi-dimensional fluorescence–Raman microscopy platform enables rapid imaging along the fluorescence emission and/or Rayleigh scatter dimensions. It is shown that optical contrast in these images can be used to select an area of interest prior to subsequent investigation with high spatially and spectrally resolved Raman imaging. This new microscopy platform combines the strengths of Raman 'chemical' imaging with light scattering microscopy and fluorescence microscopy and provides new modes of correlative light microscopy. Simultaneous acquisition of TPE hyperspectral fluorescence imaging and Raman imaging illustrates spatial relationships of fluorophores, water, lipid and protein in cells. The fluorescence–Raman microscope is demonstrated in an application to living human bone marrow stromal stem cells.

Keywords: hybrid microspectroscopy; confocal Raman imaging; two-photon excited fluorescence microscopy; Rayleigh scatter imaging; living human stem cells

Introduction

Since the first application of Raman spectroscopy and imaging on cells,[1] there have been significant developments in technology towards cell- and tissue-based applications. Spontaneous Raman imaging has been used to identify various organelles of a cell[2] and to determine the physical state of a cell, such as the viability,[3] apoptosis or necrosis,[4] dividing[5] or proliferating,[6] cancerous[7] and differentiating cell.[7]

The strength of spontaneous Raman imaging resides in the ability to generate a broad bandwidth response, which reflects the presence of many chemical parameters simultaneously. The signal-to-noise ratio is determined by the photon shot noise with a minor contribution from the detector properties. The spontaneous nature of non-coherent Raman scattering, as opposed to coherent Raman scattering processes which are enhanced by stimulated emission, gives rise to a relatively low imaging speed, however, with the advantage to obtain full spectral information during an image time frame. A combination of spectrally resolved Raman microspectroscopy with amplitude-only continuous wave (cw) two photon-excited (TPE) fluorescence microscopy has previously been shown.[8] Two-photon fluorescence was excited from an organic dye with an absorption band around 325 nm, which could be efficiently generated at the higher harmonic of the cw fundamental krypton ion laser emission at 647.1 nm. More recently, it has been shown that also fluorescence of quantum dots can be favourably combined with spontaneous Raman imaging[9] and that individual quantum dots may serve to recognize certain areas or events in a cell. Here, a new fluorescence–Raman hybrid microscopy platform is presented, which integrates (1) TPE-fluorescence 'amplitude-only' imaging, (2) low-wavenumber-resolution Raman imaging (LFRI) simultaneously with spectrally resolved cw TPE fluorescence microscopy and Rayleigh scatter imaging and (3) high wavenumber and spatially resolved confocal Raman microspectroscopy. This platform enables fast acquisition of data along fluorescence and scatter dimensions in combination with Raman chemical imaging without perturbation of the sample.

Materials and Methods

Hybrid microscope

The hybrid Rayleigh, Raman and TPE-fluorescence microscope (Fig. 1) integrates a single light source, an adapted microscope as well as different spectrographs and detector modalities. TPE-fluorescence amplitude-only imaging was performed with avalanche photodiodes (APDs) in the rapid photon counting mode (Fig. 1). A second detection branch comprises a spectrograph-1 (Fig. 1), which was optimized for broadband (344 to 1173 nm) low-wavenumber-resolved (0.1 to 1.8 nm/pixel corresponding to 7 to 22 cm^{-1}/pixel) Raman/fluorescence measurements. A third detection branch, spectrograph-2, was optimized for broadband (+20 to −3670 cm^{-1}) high-wavenumber-resolution (1.85 to 2.85 cm^{-1}/pixel) Raman microspectroscopy. The pinholes, which act simultaneously as spectrograph entrance ports in all spectrograph/detector combinations, are confocal with the same sample plane under the microscope objective. Lenses and pinholes were selected for high spatial confocal resolution at a sustainable

* *Correspondence to: Cees Otto, Biophysical Engineering Group, Biomedical Technology Institute, MESA+ Institute for Nanotechnology, University of Twente, Enschede, The Netherlands. E-mail: c.otto@utwente.nl*

Biophysical Engineering Group, Biomedical Technology Institute, MESA+ Institute for Nanotechnology, University of Twente, Enschede, The Netherlands

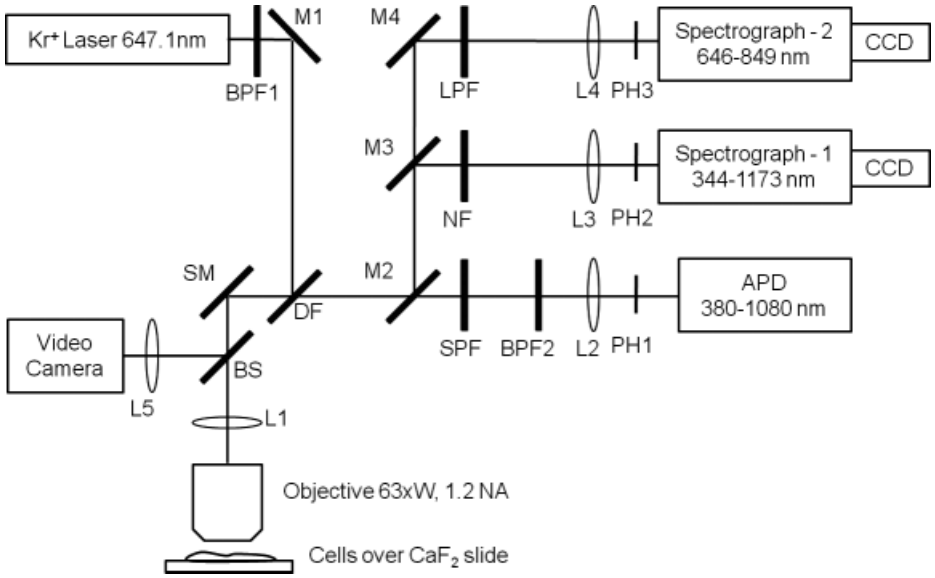

Figure 1. Illustration of hybrid Rayleigh, Raman and TPE-fluorescence microscope showing the combination of TPE confocal fluorescence microscopy, LFRI synchronous with spectrally resolved cw TPE fluorescence microscopy and Rayleigh scatter imaging and high spectral and wavenumber resolution Raman microspectroscopy. The hybrid microscope is excited with the 647.1nm line of a krypton ion laser. DF, dichroic notch filter; SM, scanning mirror; M1, M2, M3, M4, high reflectance mirrors; NF, notch filter; SPF, short-pass filter; LPF, long-pass filter; BPF1, BPF2, band-pass filter; L1, L2, L3, L4, L5, lenses with focal lengths of 100, 100, 35, 30, 75 mm, respectively; PH1, PH2, PH3, confocal pinholes of 50, 15, 15 3 m, respectively; APD, avalanche photo diode detecting in the range of 380–1080 nm; Spectrograph-1, Spectrograph-2, polychromators dispersing in the range of 344–1173 nm and 646–849 nm, respectively; CCD, CCD cameras; BS, pellicle beam splitter for monitoring bright-field micrographs of the sample and the position of the laser beam in the sample on the video camera.

loss of photons on the apertures. The design criterion for the size of the pinholes complied with a truncation of the TEM00 Gaussian beam at the $1/e^2$ points.

The detection path towards a spectrograph/detector unit was selected with foldable mirror mounts (MMF, Siskiyou, OR, USA). The mirrors were acquired from Semrock (Maxmirror, MM1-311-25, 350–1100 nm, NY, USA). A cw krypton ion laser (Coherent, Innova 90K, Santa Clara, CA; $\lambda_{emission} = 647.1$ nm) was used as a single excitation source for the optical response (TPE-fluorescence, Rayleigh scattering and Raman scattering) in the sample. A band-pass filter (BPF1 in Fig. 1; Z647BP, Chroma Technology, Rockingham, VT) was used to transmit 647.1 nm and remove laser plasma emission lines. The excitation and detection paths were separated by a dichroic beam splitter (DF in Fig. 1; Z647RDC, Chroma technology, Rockingham, VT). The beam splitter has a typical transmission of 95 and 75%, respectively, for Stokes- and anti-Stokes emitted or scattered light. The cut-on wavelength,[10] defined as the wavelength at which the transmission is 25% of the $(I_{max} - I_{min})/I_{min}$, is 660 and 625 nm on the Stokes and anti-Stokes side, respectively. A water immersion objective (Zeiss Plan, Neofluar, Carl Zeiss, Thornwood, NY; 63×, 1.2 NA) was used for illumination of the sample as well as for collection of Raman scattered photons, Rayleigh scattered photons and cw TPE fluorescence emission in the epi-detection mode.

The Raman and TPE images were obtained from three-dimensional hyperspectral (spatial × spatial × spectral) datasets, which were acquired by collecting the full spectral information from spectrograph-1 and spectrograph-2 at each step during a raster scan over the sample. The samples were scanned with a scanning mirror system (SM in Fig. 1; MG325D and G120D, General Scanning, Bedford, USA), with a position resolution of ~100 nm after magnification by the objective. Typical step sizes of 175 and 350 nm were used for the data acquired from spectrograph-1 as shown in Fig. 2, and a step size of 150 nm was used for the data acquired from spectrograph-2 as shown in Fig. 3. In cw TPE microscopy, TPE light first passes through a short-pass filter (SPF in Fig. 1; SP01-633RU, Semrock, Rochester, NY) to suppress the intense Rayleigh scattering to $\sim 10^{-5}$. This suppression factor accommodates the Rayleigh scattered signal to the dynamic range of the CCD camera that is used to detect Rayleigh scattering simultaneously with the fluorescence emission and Raman scattering. A short-pass filter followed by a 'pass through' band-pass filter (BPF2 in Fig. 1; FF01-439/154, Semrock, Rochester, NY) selects the spectral region of the fluorescence emission. The TPE photons transmitted through BPF2 are detected on an APD (APD in Fig. 1; SPCM-200/CD1705, EG&G, Optoelectronics, Fremont, California) after passing through a confocal pinhole (PH1 in Fig. 1) with a diameter of 50 µm and sample-to-pinhole magnification of 63×. The spectrograph/detector modality (spectrograph-1 in Fig.1) in low-wavenumber-resolved broadband confocal micro-spectroscopy consisted of a prism (glass type: LLF1, side 68.6mm) spectrograph and a thermo-electrically cooled CCD camera (Pixis 100B, Princeton Instruments, Roper Scientific, USA). Before entering spectrograph-1, the light passes through a super notch filter (NF in Fig. 1; <10 nm, Kaiser Optical Systems, Inc., Ann Arbor, MI), to suppress the laser line, and a confocal pinhole (PH2 in Fig. 1) with a diameter of 15 µm. The sample-to-pinhole magnification is 22×. Spectrograph-1 simultaneously acquires spectral information in TPE fluorescence, Rayleigh scattering and Stokes Raman scattering. The spectrograph covers a spectral interval from 344 to 1173 nm. This spectral range corresponds to +13 604 to −6932 cm^{-1} in relative units with respect to the excitation wavelength of the laser at 15 453.6 cm^{-1} (= 647.1 nm). The average spectral resolution per pixel varies from 12 cm^{-1} on the anti-Stokes side of the excitation wavelength to 23 cm^{-1} on the Stokes side.

Journal of RAMAN SPECTROSCOPY

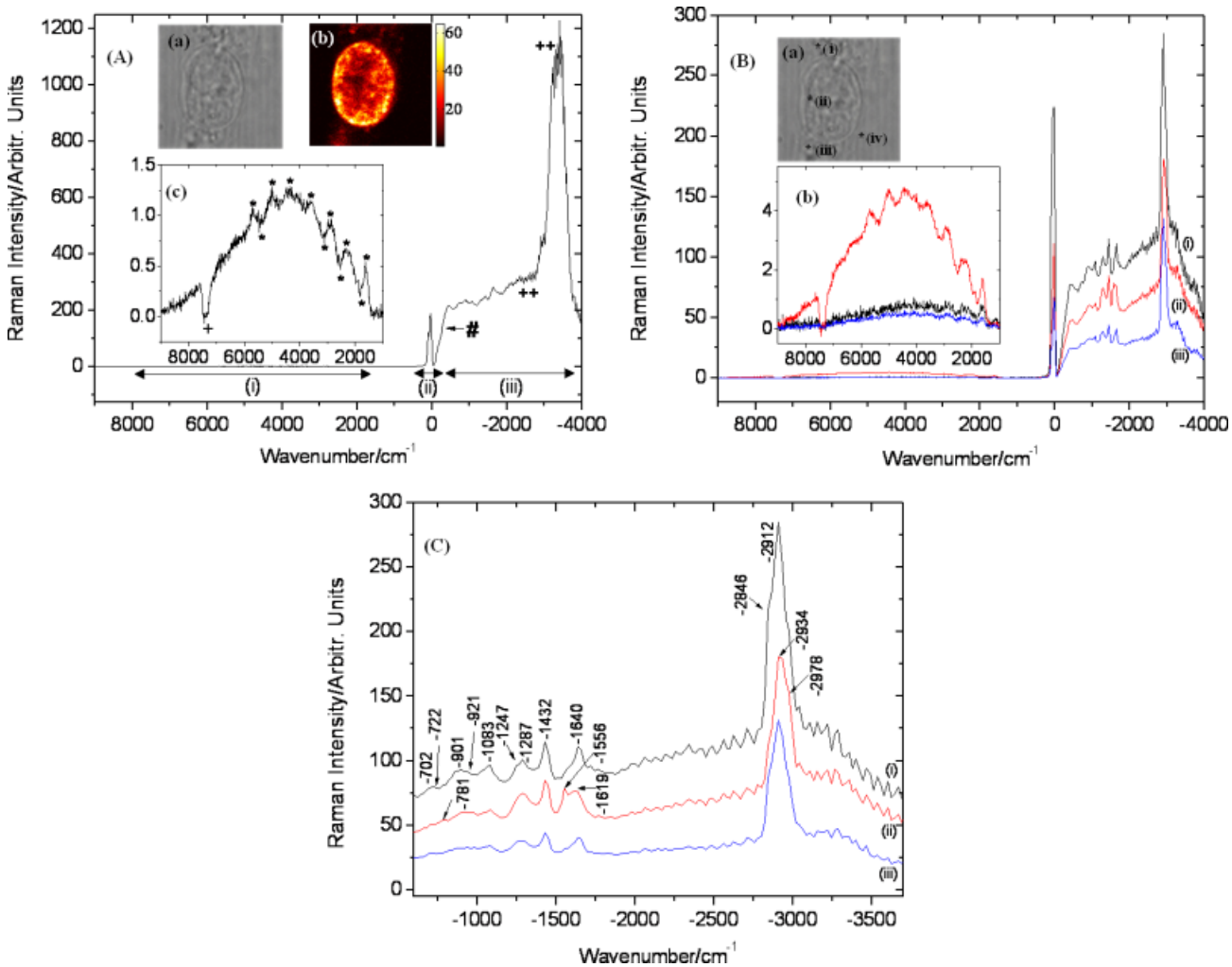

Figure 2. LFRI confocal Raman spectral information showing (A) average spectral information showing combined spectral information over region (i) TPE at anti Stokes side (left side) +9000 to +1000 cm^{-1} (409 to 608 nm)), region (ii) Rayleigh scattering (+125 to −25 cm^{-1}) and region (iii) LRRI at Stokes side (right side) (−600 to −3700 cm^{-1}); inset (a) white light micrograph of single living hBMSC cell, inset (b) nucleotide distribution in the nucleus of the living hBMSC cell obtained from cw TPE fluorescence microscopy of Hoechst-33342, Inset (c) average spectra of enlarged view of the TPE of Hoechst-33342 in the region 9000 to −1000 cm^{-1} (409 to 608 nm) as seen in region (i); (B) average spectra after background buffer subtraction obtained after HCA corresponding to (i) cytoplasm with prominent presence of lipid droplets, (ii) nucleus and (iii) cytoplasm with reduced contributions of lipids; Inset (a) white light micrograph of single living hBMSC cell showing regions of interests (i) cytoplasm with prominent presence of lipid droplets, (ii) nucleus, (iii) cytoplasm with reduced contribution of lipids and (iv) Background composed of PBS buffer. Inset (b) enlarged view of the TPE of Hoechst-33342 in the region 9000 to −1000 cm^{-1} (409 to 608 nm); (C) average spectra after background buffer subtraction obtained after HCA in the stokes region (−600 to −3700 cm^{-1}) corresponding to (i) cytoplasm with prominent presence of lipid droplets, (ii) nucleus and (iii) cytoplasm with reduced contributions of lipids.

The spectrograph/detector modality for high-wavenumber-resolution confocal Raman microscopy (spectrograph-2 in Fig. 1) records the spectral information from 646 to 849 nm in 1600 pixels on a TE-cooled electron-multiplied charged coupled device (EMCCD) (Newton DU-970N, Andor Technology, Belfast, Northern Ireland). Before entering the spectrograph-2 through a confocal pinhole (PH3 in Fig. 1) with a diameter of 15 µm and sample-to-pinhole magnification of 19×, the Raman scattered photons pass through the long-pass filter (LPF in Fig. 1; LP02-647RU, Semrock, Rochester, NY) to suppress Rayleigh scattering.

Cell culture and Hoechst 33342 staining

Human bone marrow stromal stem cells (hBMSCs) from bone marrow aspirates were obtained from healthy individuals and subsequently seeded at 1000 cells/cm^2 over UV-grade calcium fluoride (CaF_2) substrate (Crystran Ltd., UK) and cultured overnight in a Petri dish under the influence of cell culture media prepared from α-MEM (GIBCO, Carlsbad, CA), 10% fetal bovine serum (FBS; Bio Whittaker, Australia), 0.2 mM L-ascorbic acid-2-phosphate (Asap; Sigma, St. Louis, MO), 100 U/ml Pencillin G (Invitrogen, Carlsbad, CA); 100 µg/ml streptomycin (Invitrogen) and 2 mM L-glutamine (L-Glu; Sigma). hBMSCs were cultured at 37 °C in an incubator, which maintained an atmosphere of 95% humidity and 5% partial pressure of CO_2. Individual cells adhered well and spread over the CaF_2 substrate under the influence of the cell culture media. The overnight cell cultures were washed with phosphate buffer solution (PBS, GIBCO) to replace the culture media. The cells were subsequently incubated with 26 µm of Hoechst 33 342 in PBS for 20 min. The cells were then washed twice with PBS to remove excess staining. Hoechst 33 342 has a high affinity for DNA and

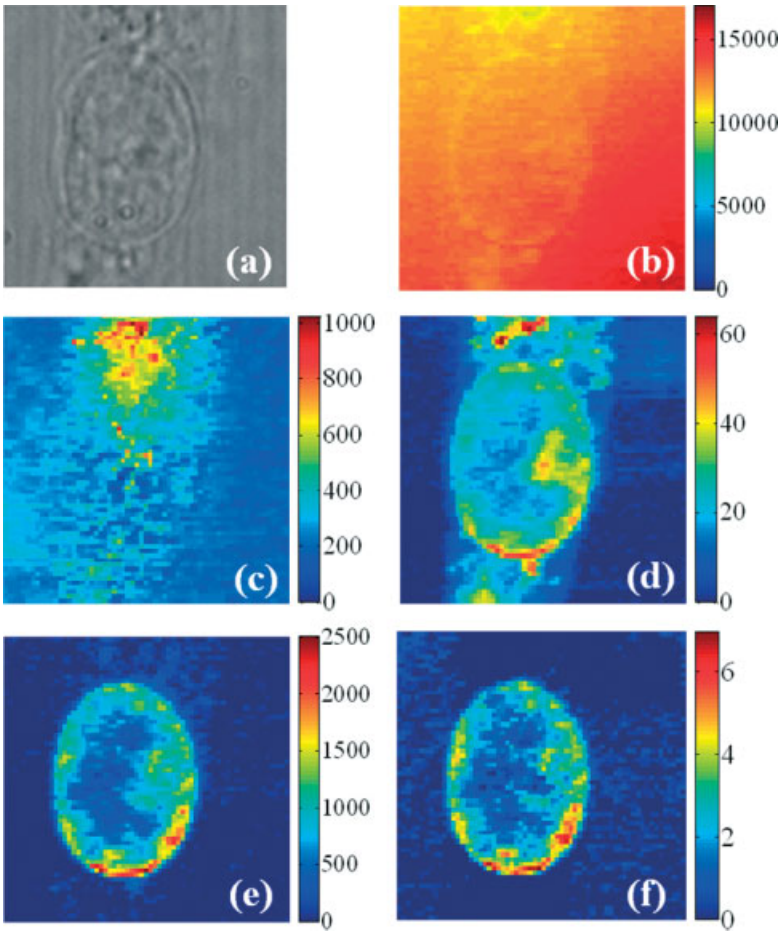

Figure 3. Hybrid microscopy images of a single living hBMSC in Physiological buffer solution. (a) White-light micrograph of single living hBMSC showing region of interest (22.5 μm × 22.5 μm) for confocal fluorescence microscopy and confocal broadband microspectroscopy. (b) Raman band integration image of high wavenumber OH vibrations around −3300 cm^{-1} band ($\Delta = 670$ cm^{-1}), (c) Band integration image over 8 pixels around 0 cm^{-1} showing Rayleigh scattering, (d) Raman band integration imaging of CH_2 deformation based on the −1430 cm^{-1} band ($\Delta = 83$ cm^{-1}), (e) Band integration image over 435 to 600 nm showing nucleotide distributions in the nucleus of the living hBMSC obtained from the cw TPE fluorescence microspectroscopy of Hoechst 33 342, (f) Raman band integration imaging of Hoechst 33 342 bound to A–T base pair DNA around −1560 cm^{-1} band ($\Delta = 41$ cm^{-1}), respectively, obtained from LFRI. The confocal fluorescence microscopy and confocal broadband microspectroscopy were acquired by scanning in 128 × 128 and 64 × 64 steps, respectively, in an area of 22.5 μm × 22.5 μm with 100 mW laser power. The imaging time for confocal fluorescence microscopy was 16 s and for confocal broadband microspectroscopy around 7 min.

results in a preferential binding particularly to the AT base pairs of DNA located in the nucleus of the cell.

Data analysis

The experimentally acquired data were converted to real Raman data by consecutive application of software that (1) removes cosmic ray events, (2) subtracts the fixed CCD camera off-set, (3) corrects for the variation in spectral transmissivity of the total set-up from the microscope objective to the CCD camera of spectrograph-2 and (4) converts the wavenumber axis from pixels to wavenumbers using the well-known bands of toluene as a calibration. All data manipulations were performed with routines written in MATLAB 7.4 (The Math Works Inc., Natick, MA). The spectral transmissivity was corrected using a tungsten–halogen light source (Avalight-HAL; Avantes BV, Eerbeek, The Netherlands) with a known emission spectrum. This correction is particularly important to remove the pronounced etalon effect inherent to back-illuminated CCD cameras. As the output of the calibration lamp is close to zero between 344 and 410 nm, no correction was applied for the spectral transmissivity obtained with spectrograph-1 (Fig. 2(a) and (b)). The spectra were organized in a matrix format with the position at which spectra are taken along the column dimension and spectral position along the row dimension. Singular value decomposition (SVD) of this data matrix was performed for all hyperspectral data cubes to reduce noise.[4,11] Univariate Raman images of the specific vibration band of interest were constructed by integrating the band intensities after local baseline subtraction. Hierarchical cluster analysis (HCA) was used as a multivariate data analysis technique to visualize the regions with high spectral similarity.[12] The results presented here are based on the inclusion of the complete spectral region from spectrograph-1 and spectrograph-2 in this analysis.

Results and Discussion

Amplitude-only cw TPE fluorescence imaging of cells labelled with Hoechst 33 342 (Fig. 2(a), inset (b), acquired with the APD branch (Fig. 1), clearly outlines the nucleus and the distribution of AT-rich chromatin in the nucleus of the cell. Relatively dark areas

Journal of RAMAN SPECTROSCOPY

in the nucleus reflect the position of the nucleoli. The apparent variation in AT-rich DNA regions illustrates the state of the cell as in the interphase. The area of the image was 22.5 μm × 22.5 μm with a pixel size of 175 nm. The pixel size corresponds to the Nyquist theorem, which states that sampling at twice the optical resolution is sufficient to acquire maximum spatial wavenumber information. Each pixel was measured during an accumulation time of 1 ms/pixel and 100 mW laser power, resulting in a dose per pixel of 100 μJ. In spite of this low dose of cw light/pixel, a pronounced non-linear response can be obtained. The image contains 128 × 128 pixels with a total image acquisition time of 16 s.

To establish a relationship between the distribution of the TPE and chemical properties of a sample, a hyperspectral dataset was acquired with spectrograph-1 (Fig. 1) after folding a mirror (M2 in Fig. 1) into the light path. The hyperspectral dataset contains spectral emission from 344 to 1173 nm, which contains spectrally resolved cw TPE fluorescence emission, Rayleigh scattering and low-wavenumber-resolved Raman scattering. Each spectrum was acquired for 100 m. The image contains 64 × 64 pixels from an area of 22.5 μm × 22.5 μm with a pixel size equal to the optical resolution of 350 nm. The total image time is 409.6 s and the effective 'voxel' volume was 0.3 femtolitre (fl). The average accumulated spectrum of all pixels is shown in Fig. 2(a), together with the white-light image (Fig. 2(a); inset (a)) and TPE fluorescence image (Fig. 2(a); inset (b)) as acquired by the APD detector (Fig. 1). Figure 2(a) (inset (c)) shows the average over all pixels of the spectrally resolved TPE amplitude region.

The spectrum in Fig. 2(a) can be divided in the following regions. Region (i) is the spectral region on the anti-Stokes side of the excitation wavelength at 647.1 nm, and the amplitude arises from photons emitted in a two-photon excited fluorescence emission process. Fig. 2(a) (inset (c)) shows a magnification of this region to which the anti-Stokes Raman spectrum potentially also contributes. Since the measurements are conducted at room temperature, the amplitude of the anti-Stokes Raman spectrum is too feeble to contribute significantly and can therefore be completely neglected under these conditions. Indicated by asterisks are spectral features caused by the transmission properties of the super notch filter that is in place to suppress the Rayleigh scattering by ~6 orders of magnitude. Furthermore, in the spectral region indicated with a '+' sign, the transmission of the super notch filter is almost zero, giving rise to a band gap in the spectrum. Region (ii) contains the Rayleigh scattering of the laser line (647.1 nm) which is transmitted by the super notch filter. The amplitude of the Rayleigh scattering is now of similar magnitude as all other signals and can be accommodated within the dynamic range of the CCD camera. Region (iii) contains the Stokes Raman spectrum. The modulation, which increases towards the 'red' edge of the spectrum indicated by '++', is a result of interference effects in the thin photosensitive layer of the back-illuminated CCD camera, commonly known as 'the etaloning effect'. The Stokes Raman spectrum is limited on the blue edge by the supernotch filter, which opens (50%) at −300 cm^{-1} as indicated by '#' in Fig. 2(a). The Stokes Raman spectrum covers 300 pixels from −300 to −6932 cm^{-1}, resulting in an average resolution of 22 cm^{-1}/pixel. The spectra are dominated by the intense Raman scattering of water throughout the spectrum with the main band of water at −3300 cm^{-1}. Even at this low resolution and in spite of the high water background, clear signals can be observed, which originate from lipid/protein distribution (−1430 to −1450 cm^{-1}) and high wavenumber OH vibrations[13] (around −3300 cm^{-1}).

HCA from +9000 to −4000 cm^{-1} of the hyperspectral dataset and subsequent subtraction of the buffer spectrum, from an area outside of the hBMSC-cell, results in the cluster spectra in Fig. 2(b). The spectra are marked as (i), (ii) and (iii) and they are representative for the corresponding locations in Fig. 2(b), inset (a). These locations also correspond to the cluster areas in the cluster image (Fig. 2(b); inset (b)). The spectra and images together suggest the following description of these regions: (i) cytoplasm with prominent presence of lipid droplets, (ii) nucleus and (iii) cytoplasm with reduced contributions of lipids and (iv) background corresponding to PBS buffer. After buffer subtraction, all cluster spectra are dominated by intense bands of the C–H stretching motion in lipids and proteins near −3000 cm^{-1}. Residual 'etaloning' is predominantly occurring above −2000 cm^{-1} in agreement with the specifications of CCD cameras. Other prominent Raman bands can be observed in the fingerprint region around −1640 cm^{-1} (water, amide I of proteins), −1556 cm^{-1} (Hoechst 33 342), −1432 cm^{-1} (lipids and proteins) and around −900 and −1100 cm^{-1} (backbone vibrations of proteins, side chain vibrations of proteins and bands of lipids). At the anti-Stokes side from +9000 cm^{-1} (409 nm) to +1000 cm^{-1} (608 nm), the TPE fluorescence emission of Hoechst is observed. As the spectra, coded by colour, belong to the same cluster, a direct relation of the spectral information in TPE fluorescence microspectroscopy (Fig. 2(b); inset (b) and Raman microspectroscopy (Fig. 2(b)) can be made. The intense TPE fluorescence emission (red spectrum) correlates with the Raman scattering from Hoechst at −1556 cm^{-1}. Minor contributions from Hoechst are still clearly visible in the 'black' and 'blue' clusters, particularly in the anti-stokes side indicated by Region (i). This contribution is due to unspecific Hoechst binding to other substrates in the cell, which is well known to occur for the incubation parameters that were used here.[14] The integrated band area intensity of the TPE fluorescence emission in the anti-Stokes region as seen in Fig. 2(b), inset (b), shows that the fluorescence of Hoechst 33 342 bound to the nucleus (red spectra) is respectively 7 and 9.5 times higher than that shown for cytoplasm with prominent presence of lipid droplets (black spectra) and cytoplasm with reduced contributions of lipids (blue spectra), respectively. The increase in fluorescence correlates with the number of molecules bound to AT base pairs of DNA in the nucleus of the cell.

In the Stokes region, shown in Fig. 2(c), the spectra show bands at −702, −722, −781, −901, −921, −1083, −1247, −1287, −1432, −1556, −1619, −1640, −2846, −2912, −2934 and −2978 cm^{-1}, which signify the molecular composition corresponding to proteins, lipids and nucleotides in the region of interest. These spectral markers merely indicate the wavenumber assignment to the pixel and not the 'true' position of this band, since in the low-wavenumber-resolved mode a pixel corresponds, on average, to 22 cm^{-1}. The cluster spectrum in Fig. 2(b)(i) shows prominent strong bands at positions −901, −1083, −1640, −2846 (shoulder band) and −2912 cm^{-1}, which confirms the presence of lipids. The presence of bands at −781 and −1556 cm^{-1} in the cluster spectrum of Fig. 2(b)(ii) corresponds to nucleotides and Hoechst 33 342 bound to AT base pairs of DNA in the nucleus of the cell. The presence of bands around −1619, −2934 and −2978 cm^{-1} (shoulder band) signifies the occurrence of proteins in the nucleus of the cell. The same spectrum in the anti-Stokes region shows intense TPE fluorescence emission due to Hoechst 33 342, which is in agreement with the Raman spectrum. The Stokes region of the

spectrum in Fig. 2(b)(iii) shows bands at similar positions as that seen in Fig. 2(b) (i); however, the bands are much weaker, which reflects a lower lipid and protein concentration in the region under consideration.

Naturally, the relatively low-wavenumber-resolved Raman microspectroscopy datasets convey less molecule-specific information as do high-resolution Raman microspectroscopy data (*vide infra*). The Raman spectra are, however, distinctive enough to extract useful amplitudes for correlation imaging. In Fig. 3, Raman images are prepared from the hyperspectral dataset. The distribution of water in Fig. 3(b), Rayleigh scattering in Fig. 3(c), lipids/proteins in Fig. 3(d), spectrally resolved TPE fluorescence in Fig. 3(e) and Raman scattering from Hoechst 33 342 in Fig. 3(f) are shown together with the white-light image in Fig. 3(a). The spectrally resolved cw TPE fluorescence image (Fig. 3(e)) correlates well with the amplitude-only cw TPE fluorescence image shown in the inset Fig. 2(a), inset (b) and the Raman scattering from Hoechst in Fig. 3(f), as expected. The Raman image for the band at about $-1432\ cm^{-1}$ in Fig. 3(d) shows the distribution of lipids/proteins in a cell. The Rayleigh scattering image (Fig. 3(c)) is constructed from the amplitude in eight pixels around $0\ cm^{-1}$ and shows the location of highly scattering areas in the cell, such as the endoplasmic reticulum. Cell organelles composed of lipids contribute strongly to Rayleigh scattering as a result of relatively large variation of the refractive index of those organelles with the surrounding cytoplasm. The Rayleigh scattering image from highly scattering, lipid-rich heterogeneous areas anti-correlates with the image of the high wavenumber OH stretch vibration around $-3300\ cm^{-1}$ (Fig. 3(b)). The understanding behind this observation is that lipid-rich areas are relatively low in water content. The relatively high Rayleigh scattering for lipid-rich regions in the cytoplasm correlates positively with the Raman band integration image constructed from the amplitude around $-1432\ cm^{-1}$, which corresponds to the CH_2 deformation mode of lipids/proteins in Fig. 3(c) and (d), respectively.

Figure 4(a), (b) and (c) shows the two-level HCA over the hyperspectral data acquired from spectrograph-1 in spectral region corresponding to TPE at anti-Stokes region (+9000 to $+1000\ cm^{-1}$), Rayleigh scattering (8 pixels around $0\ cm^{-1}$) and low-resolution Raman imaging at Stokes region (-600 to $-3700\ cm^{-1}$), respectively. Two-level cluster analysis indicates that the hyperspectral dataset was clustered up to two clusters. Two-level cluster analysis is a useful method to identify the object in the buffer environment. The average spectra for each cluster image presented in Fig. 4(a) and (c) are shown in Fig. 4(d) and (e). The two-level HCA image of spectral information in the range -9000 to $-1000\ cm^{-1}$ clearly outlines the nucleus. Black pixels in the nucleus locate the nucleolus, which is characterized by a relatively low DNA content and therefore a low contribution of Hoechst 33 342. The spectrum corresponding to the grey cluster in Fig. 4(a) is shown in Fig. 4(d). The cluster assigned by grey pixels in Fig. 4(a) corresponds to images shown in Fig. 2(a), inset (b) and Fig. 3(e), respectively, to cw TPE fluorescence microscopy image from APD and band integration image of cw TPE fluorescence spectroscopic data from spectrograph-1 in the anti-Stokes region. The two-level HCA image over the range corresponding to Rayleigh scattering is shown in Fig. 4(b). The cluster image (grey pixels) shows a similar pattern as observed in Fig. 3(c) and (d), which corresponds to band integration image for the Rayleigh band and the $1430\ cm^{-1}$ band for CH_2 deformation of lipids/proteins. The high-intensity regions in Fig. 3(c) and (d) are in good agreement with the grey cluster. The spectra corresponding to grey pixels show higher intensity because of the higher scattering capabilities of lipid-based organelles compared to the spectra of pixels corresponding to the black cluster which reflect the more aqueous cytoplasmic area in the cell and PBS buffer media as seen in Fig. 4(b). Two-level HCA image over the Stokes region from -600 to $-3700\ cm^{-1}$ shows low-wavenumber-resolution Raman imaging as seen in Fig. 4(c), and the respective average cluster spectra are shown in Fig. 4(e). The grey and black clusters relate to the complete cell

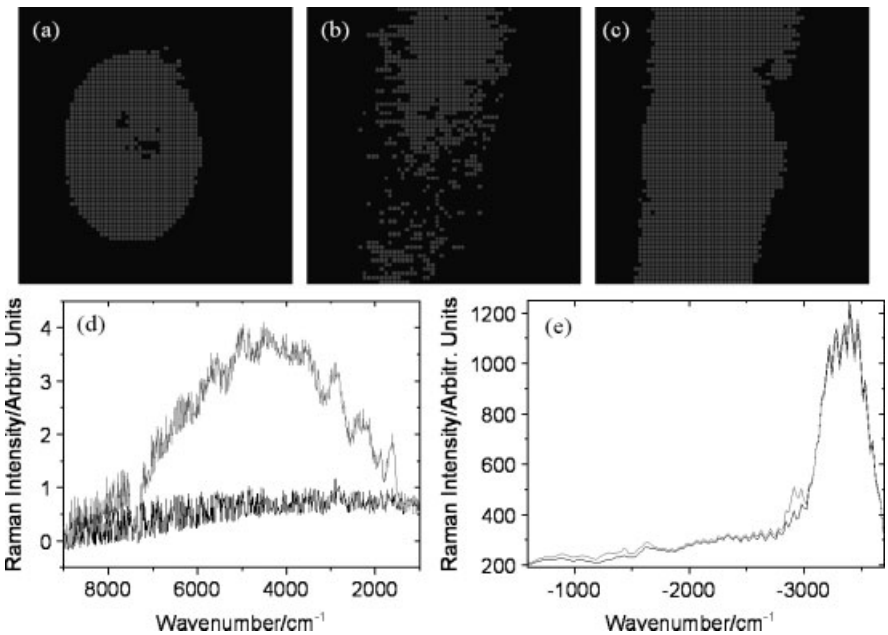

Figure 4. Raman cluster images after two level HCA of the acquired hyper spectral data from the living hBMSC shown in Fig 2(a) over the spectral region corresponding to (a) TPE at anti Stokes side (+9000 to $+1000\ cm^{-1}$), (b) Rayleigh scattering (8 pixels around $0\ cm^{-1}$), (c) low resolution Raman imaging at stokes region (-600 to $-3700\ cm^{-1}$), (d) average spectra of all pixels corresponding to respective cluster seen in (a) for anti Stokes region, and (e) average spectra of all pixels corresponding to respective cluster seen in (c) for Stokes region.

Journal of RAMAN SPECTROSCOPY

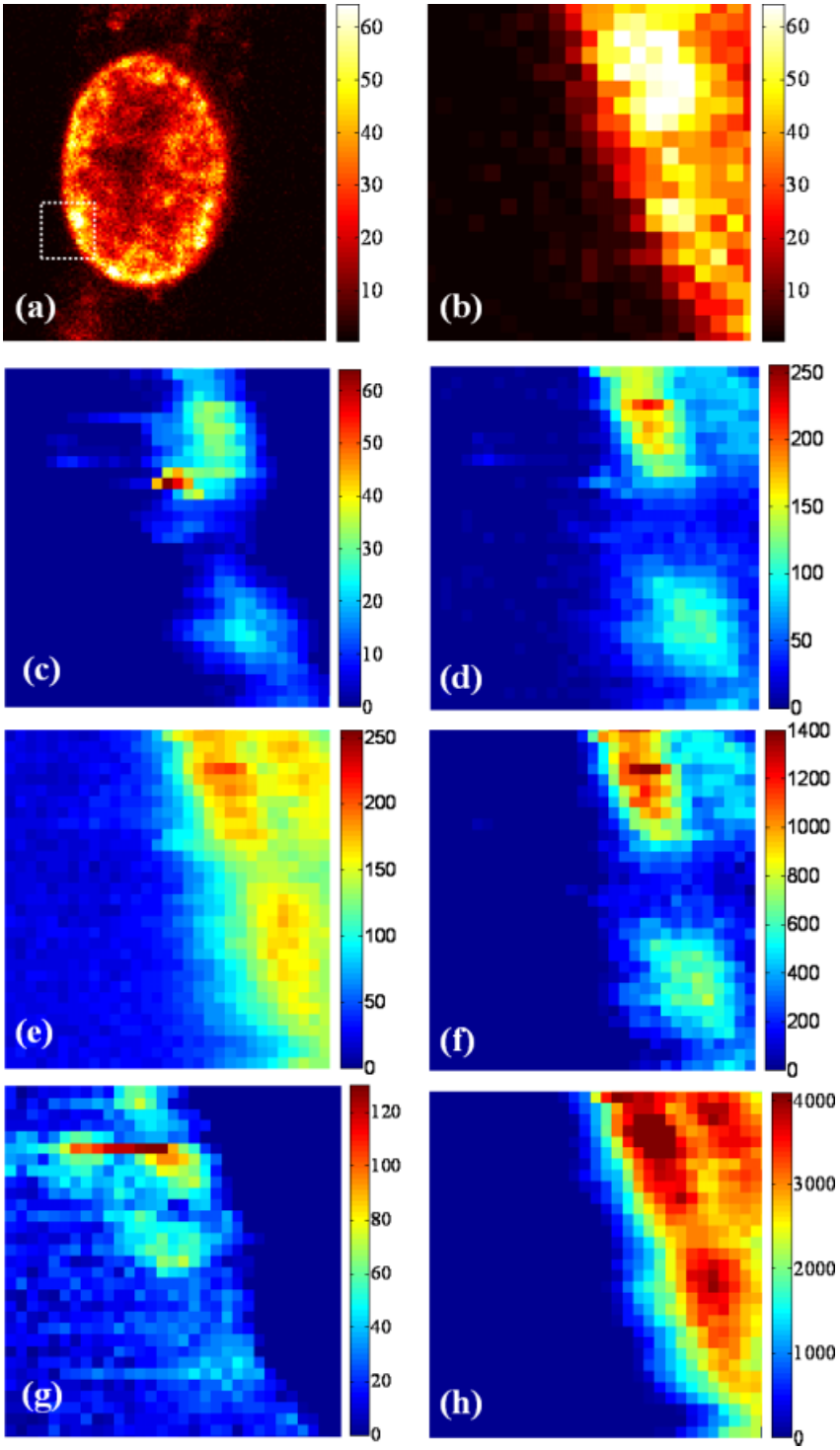

Figure 5. Hybrid microscopy images of a single living hBMSC in physiological buffer solution obtained from high-wavenumber-resolution Raman microspectroscopy. (a) Nucleotide distribution in the nucleus of the living hBMSC obtained from cw TPE fluorescence microscopy of Hoechst 33 342. (b) Enlarged view of the region of interest from Fig. 5(a) (4.9 μm × 4.9 μm, white dotted line) for high-wavenumber-resolution confocal Raman microspectroscopy. (c) Raman imaging for C–N of membrane lipids around −717 cm^{-1} band (Δ = 29 cm^{-1}). (d) Raman imaging for backbone O–P–O of DNA around the −785 cm^{-1} band (Δ = 35 cm^{-1}). (e) Raman imaging for phenylalanine around the −1003 cm^{-1} band (Δ = 25 cm^{-1}). (f) Raman imaging for Hoechst 33 342 bound to A–T regions of the nucleus around the −1560 cm^{-1} band (Δ = 68 cm^{-1}). (g) Raman imaging for CH_2 antisymmetric stretch of lipids around the −2890 cm^{-1} band (Δ = 76 cm^{-1}). (h) Raman imaging for CH_2 antisymmetric stretch of protein around the −2935 cm^{-1} band (Δ = 120 cm^{-1}). The high-wavenumber-resolution Raman microspectroscopy images were acquired by scanning in 32 × 32 steps, respectively, in an area of 4.9 μm × 4.9 μm with an imaging time around 9 min and 100 mW laser power.

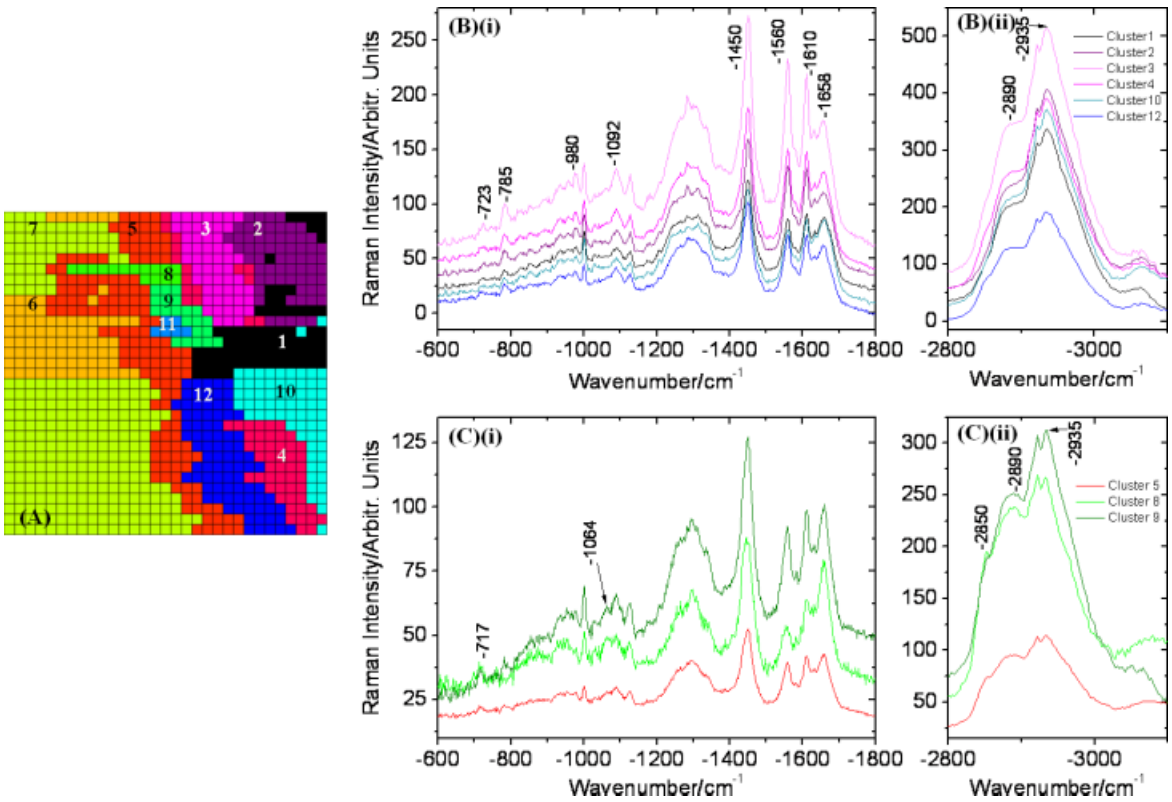

Figure 6. High wavenumber resolution confocal Raman spectral information showing (A) Hierarchical cluster analysis up to 12 cluster levels over the region of interest shown in Fig 5a. (B) Average spectra after background buffer subtraction for clusters 1, 2, 3, 4, 10 and 12 shown over the (i) finger print region (−600 to −1800 cm^{-1}), and (ii) high wavenumber region (−2800 to −3100 cm^{-1}) indicating prominent bands for nucleotides and Hoechst-33342 bound to AT base pair of DNA of nucleus of the cell; and (C) average spectra after background buffer subtraction for clusters 5, 8, and 9 shown over the (i) finger print region (−600 to −1800 cm^{-1}), and (ii) high wavenumber region (−2800 to −3100 cm^{-1}) indicating significant bands for membrane lipid phosphatidylcholine and lipids respectively.

in the region of interest and PBS buffer signifying background, respectively. The distribution of grey pixels corresponds to the hBMSC, whose white-light micrograph is shown in Fig. 2(a), inset (a) and is similar to band integration image of the −1432 cm^{-1} band for CH_2 deformation of lipids/proteins as seen in Fig 3(d). The average spectra of all the pixels corresponding to grey pixels show prominent bands at −722, −781, −921, −1083, −1287, −1432, −1640, and −2934 cm^{-1} corresponding to proteins, lipids and nucleotides as seen in Fig. 4(e) unlike the average spectra of pixels corresponding to the black cluster. The grey cluster obtained from two-level HCA over different spectral regions shown in Fig. 4(a), (b) and (c) is influenced by the chemical variations in the hBMSC under consideration.

The results from confocal fluorescence microscopy and confocal broadband microspectroscopy enable selection of regions of interest for high wavenumber and spatially resolved Raman microspectroscopy as shown in Fig. 5(a) (white dotted line) obtained from spectrograph-2. An area of 4.9 μm × 4.9 μm was selected to contain a recognizable area in the nucleus, the curved shape of the nuclear membrane and an area in the cytoplasm. Figure 5(b) shows the enlarged view of the region of interest that is shown in Fig. 5(a). High wavenumber and spatially resolved Raman spectroscopy was achieved by folding the mirrors M2 and M4 (Fig. 1). The area was imaged with a pixel size of 150 nm, an accumulation time of 500 ms/pixel and a laser power of 100 mW, which results in a total imaging time of ∼8 min. The high wavenumber resolution in the hyperspectral Raman dataset has now been used to generate univariate images of bands at −717, −785, −1003, −1560, −2845 and −2935 cm^{-1}, respectively in Fig. 5(c), (d), (e), (f), (g) and (h)). These bands correspond, respectively, to membrane lipids, DNA, phenylalanine, Hoechst 33 342 molecules, lipids and proteins.[13,15–17] The band integration image of Hoechst 33 342 at −1560 cm^{-1} (Fig. 3(f)) corresponds to the Raman image (Fig. 5(d)) for DNA, which is in accordance with expectation, based on the fluorophore interaction with DNA. The Raman image (Fig. 5(e)) for the band at −1003 cm^{-1} shows the distribution of phenylalanine over the cell, which is in accordance with the Raman image for the protein distribution derived from the band around −2935 cm^{-1} (Fig. 5(h)), as must be expected. The Raman image for the band at −2845 cm^{-1} (Fig. 5(g)) shows the distribution of lipids. The Raman image (Fig. 5(c)) for membrane phospholipids characterized by a band at −717 cm^{-1} represents the distribution of phosphatidylcholine.

The univariate images can be compared with the HCA image in Fig. 6(a). This figure shows 12 levels of cluster analysis of the hyperspectral data acquired from the region of interest (dotted white line in Fig. 5(a)) of 4.9 μm × 4.9 μm with a pixel resolution of 150 nm. The clusters marked with numbers 1 to 5 and 8 to 12 correspond to major cellular features, and clusters 6 and 7 correspond to the background PBS buffer, with a minor difference in the intensity of the water band around 3300 cm^{-1} in cluster 6. The influence of PBS is removed from each cluster by subtracting the average spectra of all pixels corresponding to cluster 6 and 7 with the average spectra obtained from pixels corresponding

Journal of RAMAN SPECTROSCOPY

to other respective clusters. Fig. 6(b) (i) and 6(b) (ii) show the background-free spectra for the clusters 1, 2, 3, 4, 10 and 12 in the fingerprint region and high wavenumber region, respectively. The intense bands at −980, −1450, −1560, −1610 and −1658 cm^{-1} in the fingerprint region (Fig. 6(b) (i)) correspond to Hoechst 33 342 molecule bound to AT base pairs in DNA.[8] The band at −1560 cm^{-1} observed in the data acquired from spectrograph-2 is also observed in the data acquired from spectrograph-1 at a pixel with wavenumber assignment −1556 cm^{-1} (Fig. 2(ii)). The bands at the positions −723 and −1092 cm^{-1} correspond to the presence of adenine molecule and nucleic acid phosphate backbone, respectively. The highest intensity in these bands is shown by cluster 3 (magenta color pixels), which corresponds to an area with a high density of DNA in the nucleus. This area corresponds well with the amplitude-only cw TPE fluorescence microscopy image and to the pixels corresponding to the univariate Raman images for backbone O–P–O of DNA band around −785 cm^{-1} (Fig. 5(b) and (d)), respectively. The bands around −1658 and −2935 cm^{-1} in Fig. 6(b) (i) and 6(b)(ii) signify the occurrence of proteins in the region of interest.

The background-free spectra associated with clusters 5, 8 and 9 for the fingerprint region and the high wavenumber region, respectively, are shown in Fig. 6(c) (i) and 6(c)(ii). There are prominent bands at −1450, −1560 and −1610 cm^{-1} (Fig. 6(c) (i)); however, these bands are weaker than the same bands represented in Fig. 6(b)(i). The presence of a band at −717 cm^{-1} signifies the presence of membrane lipid phosphatidylcholine.[13] The region over the clusters 5, 8 and 9 correspond to the membrane as can be observed from the presence of the −717 cm^{-1} and the absence of the −723 cm^{-1} band for nucleotide. The assignment of these clusters to lipid-rich nuclear membrane is further supported by −1064 cm^{-1} for skeletal C–C stretch of lipids in Fig 6(c) (i) and by bands in the high wavenumber region at −2850 cm^{-1} in Fig. 6(c)(ii), which are not present in the spectra corresponding to nucleus (Fig. 6(b)(ii)). The area of the clusters 5, 8 and 9 corresponds to the pixels in the univariate Raman image for the band around −717 cm^{-1} (Fig. 5(c)) and the Raman image for the CH_2 antisymmetric stretch mode of lipids around −2890 cm^{-1} band (Fig 5(g)), respectively.

The univariate images in Fig. 5 are in good correspondence with the images after cluster analysis (Fig. 6(a)). Since the spectral information of the nuclear region in Fig. 6(b) and (c) is dominated by variations in the concentration of Hoechst 33 342, it is interesting to quantify the difference. We have defined ratio spectra R from cluster spectra (i) and (j), respectively $C_i(\nu)$ and $C_j(\nu)$, as follows:

$$R(\nu) = \frac{C_i(\nu) - C_j(\nu)}{(C_i(\nu) + C_j(\nu))}$$

Defined in this way, the ratio spectrum reflects the percentage variation with respect to the average of spectrum (i) and (j). Figure 7(a) shows the ratio spectrum of the cluster area $i = 3$ and $j = 12$, where $i = 3$ is a region with high DNA concentration and $j = 12$ is an area with relatively low DNA concentration. The Raman bands for Hoechst 33 342 are visible at an excellent signal-to-noise ratio. The negative value of the OH band in the ratio spectrum around −3300 cm^{-1} indicates the decrease of water in areas of higher concentration of DNA: here in cluster 3 as compared to cluster 12. The ratio spectrum for the presence of membrane lipids over the clusters 5 and 8 corresponding to minimum and maximum distribution is shown in Fig. 7(b). The ratio spectrum shows a significant

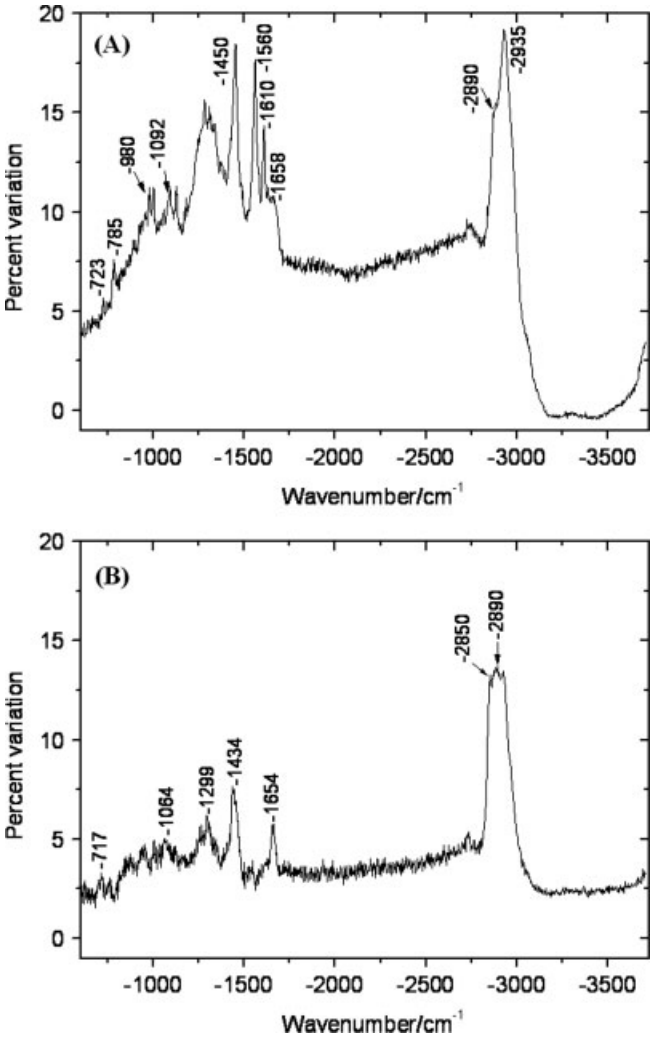

Figure 7. Ratio spectroscopy showing percentage variation over the 12-level cluster image showing the maximum and minimum distribution of molecules: (a) Percentage variation of Hoechst 33 342 bound the A–T base pairs of DNA over the pixels corresponding to cluster 3 and cluster 12 for maximum and minimum distribution, respectively; (b) Percentage variation of membrane lipids present over the pixels corresponding to cluster 8 and cluster 5 for maximum and minimum distribution, respectively.

band at −717 cm^{-1} for phosphatidylcholine and other bands that can be assigned to lipids at −1064, −1299, −1434, −1654 and −2850 cm^{-1} similar to that seen in Fig. 6(c) (i) and 6(c)(ii). The presence of the OH band around −3300 cm^{-1}, which is almost of same intensity as the baseline, indicates similar amounts of water over the clusters corresponding to lipid membranes.

Conclusion

We have presented a flexible and versatile Rayleigh/Raman/fluorescence microscope system, which is based on a single laser emission wavelength of 647.1 nm. This system comprises three detection modalities, which are all confocal with the same sample plane. The three detection modalities include the following: (1) A detector for an amplitude-only TPE fluorescence microscopy; (2) A low- wavenumber-resolution

prism spectrograph covering a bandwidth from 344 to 1173 nm, which offers a spectrally resolved TPE signal, a Rayleigh scatter signal and a spectrally resolved, low resolution Raman signal: all signals fall within the dynamic range of the CCD camera, and it has been shown (*vide supra*) that all signals can be simultaneously acquired within a single camera read-out; (3) A high-resolution hyperspectral Raman detection system covering a bandwidth of 646 to 849 nm, which corresponds to a Raman spectrum from $+20\,cm^{-1}$ to $-3670\,cm^{-1}$. The strength of the fluorescence/Raman microscope is that fluorescence microscopy, as a 'gold standard' microscope method in biology, can be combined with Raman and Rayleigh scattering microscopy. The latter microscopic techniques give complementary information on the chemical composition and the light scattering, respectively, from spatially correlated events. The development of hybrid microscopy techniques has acquired intense interest currently, precisely because of their ability to correlate diverse molecular properties through distinct optical signals.[8,18,19]

We have furthermore shown that amplitude-only cw-TPE (modality 1) provides a fast and easy way to scan a large field of view that enables subsequent selection of areas of interest for detailed investigation with Rayleigh and Raman scattering. A subsequent measurement with modality 2 acquires in a single camera read-out the spectrally resolved TPE emission, the Rayleigh scattering at $0\,cm^{-1}$ and the low-wavenumber-resolved Raman imaging (LFRI). This mode offers strict image correlation between diverse optical signals. All information from modalities 1 and 2 is available to zoom on to an area of interest for high-spatial-resolution Raman imaging. Raman images were acquired that fulfill the Nyquist theorem at an optical far-field resolution of approximately 370 nm. The Rayleigh/Raman/fluorescence microscope was exemplified in an application to living bone-marrow-derived human MSCs.

Acknowledgement

Financial support of the Dutch Program for Tissue Engineering through grant number TGT.6737 is gratefully acknowledged.

References

[1] G. J. Puppels, F. F. M. de Mul, C. Otto, J. Greve, M. Robert-Nicoud, D. J. Arndt-Jovin, T. M. Jovin, *Nature* **1990**, *347*, 301.
[2] N. Uzunbajakava, A. Lenferink, Y. Kraan, B. Willekens, G. Vrensen, J. Greve, C. Otto, *Biopolymers* **2003**, *72*, 1.
[3] I. Notingher, S. Verrier, H. Romanska, A. E. Bishop, J. M. Polak, L. L. Hench, *Spectrosc. Int. J.* **2002**, *16*, 43.
[4] N. Uzunbajakava, A. Lenferink, Y. Kraan, B. Willekens, G. Vrensen, J. Greve, C. Otto, *Biophys. J.* **2003**, *84*, 3968.
[5] C. Matthäus, S. Boydston-White, M. Miljković, M. Romeo, M. Diem, *Appl. Spectrosc.* **2006**, *60*, 1.
[6] K. W. Short, S. Carpenter, J. P. Freyer, J. R. Mourant, *Biophys. J.* **2005**, *88*, 4274.
[7] I. Notingher, G. Jell, U. Lohbauer, V. Salih, L. L. Hench, *J. Cell. Biochem.* **2004**, *92*, 1180.
[8] N. Uzunbajakava, C. Otto, *Opt. Lett.* **2003**, *28*, 2073.
[9] H. J. van Manen, C. Otto, *Nano Lett.* **2007**, *7*, 1631.
[10] P. M. Froehlich, G. G. Guilbault, Instrumentation for fluorescence, in *Practical Fluorescence* (2nd edn), (Ed.: G. G. Guilbault), CRC Press: New York, **1990**, pp 41.
[11] N. Uzunbajakava, J. Greve, C. Otto, *Proc. SPIE* **2003**, *4963*, 223.
[12] H. J. van Manen, Y. M. Kraan, D. Roos, C. Otto, *Proc. Natl. Acad. Sci. U S A* **2005**, *102*, 10159.
[13] C. Krafft, L. Neudert, T. Simat, R. Salzer, *Spectrochem. Acta, Part A* **2005**, *61*, 1529.
[14] H. M. Shapiro, *Practical Flow Cytometry* (4th edn), John Wiley & Sons: New Jersey, **2003**.
[15] W. Peticolas, W. Kubasek, G. Thomas, M. Tsuboi, Nucleic acids, in *Biological Applications of Raman Spectroscopy*, vol. 1 (Ed.: T. G. Spiro), Wiley: New York, **1987**, pp 81.
[16] A. T. Tu, *Raman Spectroscopy in Biology: Principles and Application*, Wiley: New York, **1982**.
[17] F. Zimmermann, B. Zimmermann, J. Panitz, A. Wokaun, *J. Raman Spectrosc.* **1995**, *26*, 435.
[18] H. Chen, H. Wang, M. N. Slipchenko, Y. K. Jung, Y. Shi, J. Zhu, K. K. Buhman, J. X. Cheng, *Opt. Express* **2009**, *7*, 1282.
[19] M. Krause, P. Rösch, B. Radt, J. Popp, *Anal. Chem.* **2008**, *80*, 8568.